www.sciencemag.org/content/356/6344/1276/suppl/DC1

# Supplementary Material for

## Metalloprotein entatic control of ligand-metal bonds quantified by ultrafast x-ray spectroscopy

Michael W. Mara, Ryan G. Hadt, Marco Eli Reinhard, Thomas Kroll, Hyeongtaek Lim, Robert W. Hartsock, Roberto Alonso-Mori, Matthieu Chollet, James M. Glownia, Silke Nelson, Dimosthenis Sokaras, Kristjan Kunnus, Keith O. Hodgson, Britt Hedman, Uwe Bergmann, Kelly J. Gaffney, Edward I. Solomon*

*Corresponding author. Email: edward.solomon@stanford.edu

Published 23 June 2017, *Science* **356**, 1276 (2017)
DOI: 10.1126/science.aam6203

**This PDF file includes:**

**Supplementary Text.**

**S.1 Materials and Methods.**

***S.1.1 Sample Preparation***. Solutions of horse heart cyt *c* was purchased from Sigma-Aldrich, and solutions were prepared at 4 mM in 100 mM, pH 7.2 phosphate buffer. Cyt *c* was purified by FPLC on a cation exchange column using NaCl as elutant. Purified protein was then dialyzed for ~24 hours and then concentrated to 4 mM, as determined by UV-Vis Spectroscopy. Solutions were reduced using sodium dithionite immediately before the experiment; the UV-Vis spectrum was collected after adding dithionite to confirm complete reduction (i.e. appearance of 520 nm and 550 nm bands, disappearance of 695 nm band.)

***S.1.2 Experimental Procedures.*** Ultrafast hard X-ray spectroscopy measurements were performed at the X-ray Pump Probe (XPP) instrument(*41*) at the Linac Coherent Light Source (LCLS). The sample was flowed using an HPLC pump through a 100 µm inner diameter capillary to form a 100 µm diameter cylindrical liquid jet; the sample was probed shortly after exiting the capillary in the region where laminar flow was achieved. The jet was held in a sealed environment under helium atmosphere, preventing oxidation to ferric cyt *c*. The sample was excited nearly collinearly with a 50 fs FWHM, 520 nm laser beam (~20 mJ/cm$^2$) generated by optical parametric amplification of the 800 nm output of a Ti:sapphire regenerative amplifier laser system (Coherent, Legend). The 520 nm beam was at the peak of the β-band of the heme. The pump laser fluence was determined by a power titration measurement at the beginning of the experiment and chosen to maximize the excited-state fraction while minimizing multi-photon absorption effects. The actual time delay between the laser and XFEL pulse was determined via the timing tool installed at XPP. The 50 fs FWHM X-ray laser pulses were focused using Be compound refractive lenses to a 50 µm diameter spot size on the sample jet. The Kβ-XES measurements utilized 8 keV self-amplified stimulated emission (SASE) X-ray pulses. For the K-edge XAS, a channel-cut monochromator with Si(111) crystals (~1 eV resolution) was used to scan over the energy range of 7.104 to 7.24 keV.

The incoming X-ray pulse was measured using non-invasive diagnostics before the sample. A high-energy resolution energy dispersive X-ray emission spectrometer, based on the von Hamos geometry, was used to capture the Fe 3p → 1s fluorescence(*42*). The spectrometer was equipped with 4 cylindrically bent (0.5 m radius) Ge(620) crystal analyzers and set to cover the Bragg angle range from 78.0° to 80.4°. The CSPAD 2D pixel array detector (388 x 370 pixels) intersected the X-rays diffracted from the crystal in an energy range from 7.033 to 7.084 keV.

***S.1.3 Processing and Normalization of K-edge XAS Data.*** K-edge XAS data were collected in two portions: the first covered the pre-edge and edge regions, from 7.033 to 7.1355 keV, while the second covered the shape resonance, from 7.122 to 7.24 keV. Full range scans were constructed by splicing together these two portions, with each portion superimposed in the overlapping region of 7.122-7.1335 keV. In order to avoid any abnormalities in the data from this process, and to ensure proper normalization over the small energy range used, a steady-state ferrous cyt *c* Fe K-edge XAS spectrum was collected at beamline 7-3 of the Stanford Synchrotron Radiation Lightsource (SSRL), which was normalized using the standard spline fitting method in PySpline(*43*). The **GS** spectrum was then scaled up to the steady-state spectrum by subtracting out a linear background and multiplying by a scaling factor to ensure a good match to the steady-state spectrum (Figure S7). The laser on spectrum was spliced and scaled using the same process, and we confirmed that the relative changes between the **GS** and

laser on spectra were properly conserved following this process. The laser on spectrum was treated as a linear combination of **GS** and **ES** spectra, and the **ES** spectrum was obtained by subtracting out the **GS** component, as determined from the Kβ XES kinetic modeling below.

***S.1.4 Computational Methods.*** Models for the six-coordinate, low-spin and five-coordinate, high-spin cyt *c* were generated by DFT calculations. Ground state geometry optimizations were performed using Gaussian 09(*44*), with the unrestricted functional BP86, modified to include Hartree-Fock (HF) mixing of 20% with a triple-zeta (6-311G*) basis set on Fe, N and S, and a double-zeta (6-31G*) basis set on all other atoms, as used in our previous study.(*14*) The general model used is shown in Fig. 1b. This model includes the propionate and crosslinked cysteine side chains on the heme, as well as Tyr(67) and Pro(30) fragments due to their H-bonding interactions with the Met(80) and His(18), respectively. Because ground-state DFT calculations overestimated the Fe-S(Met) bond distance, the Fe-S(Met) bond distance for the six-coordinate model was fixed to its EXAFS bond distance of 2.29 Å.(*9*) For photoexcited species models, calculations were set to high-spin, and restrictions on the Fe-S(Met) distance were released. Additional models were generated by fixing the Fe-N(His) and Fe-S(Met) at various distances. Using the generated DFT models, the corresponding K-edge XAS spectra were constructed using the multiple-scattering XANES simulation package MXAN(*26*, *27*). The geometry optimized DFT models were used without additional structural optimization in MXAN, and the best simulation was chosen based on the $\chi^2$ residual between the calculated and experimental spectra; the best fit spectra are shown in Figure 1c,d, while the remaining simulations are shown in figures S2-S8. For determination of the hydrogen-bonding network enthalpy contribution, DFT calculations were performed as above, with the addition of Asn-52, Thr-78, and $H_2O$ (Fig. 3d and Fig. S11).

***S.1.5 Extraction of X-ray emission spectra from the Cornell-SLAC Pixel Array Detector (CSPAD).*** The region of interest (ROI) on the detector area was defined as a rectangular box centered on an adequate ROI center along the nondispersive axis and comprising all 388 pixels along the dispersive axis. The width was chosen to be five pixels to ensure highest spectral resolution. A background ROI shifted by 19 pixels along the non-dispersive axis was defined with the same width, and counts were subsequently summed along the non-dispersive direction in both ROI's and the difference was taken. The same ROI parameters were used at each time delay.

All spectra were area-normalized independently at each time delay. The **GS** spectrum was then defined as the average spectrum before time zero and energy calibration was done by mapping the off-spectrum onto a singlet reference spectrum(*22*).

***S.1.6 Estimation of the time-dependent quintet state fraction.*** In the following, the quintet state population is estimated without imposing any kinetic model. Generally, the excited state populations at any given pump-probe delay can be estimated from fitting the transient spectrum with a linear combination of differences constructed from reference spectra of different spin multiplicities (Fig. S9). The scaling factors reflect the respective excited state populations as a function of pump-probe delay.

After one picosecond, the transient spectra predominantly decay in amplitude without any further apparent spectral evolution. This is confirmed by a singular value decomposition which satisfactorily describes the data with a single component. Therefore, at each time delay the transient was first fitted with a single scaled reference difference spectrum taking into account

the fact that the photolysis yield cannot exceed one. Only the quintet state is considered and optimization was performed at every time delay $\Delta t_j$ by minimizing the following expression.

$$\sqrt{\frac{\sum_{i=1}^{N_E}\left(XES(E_i,\Delta t_j)-\alpha(\Delta t_j)\cdot(Q(E_i)-S(E_i))\right)^2}{N_E-m}} \quad (1)$$

$N_E$ is the number of energy points $E_i$. $Q$ and $S$ are the quintet and singlet spin states and $m$ = 1 is the number of fit parameters (scaling factor $\alpha$.) $XES$ represents the noise-filtered data resulting from a singular value decomposition.

The resulting quintet (and singlet) state populations are shown in Fig. 3c inset.

***S.1.7 Modeling of the Met recombination thermodynamics.*** Previous ultrafast measurements of ferrous cyt *c* revealed that, following Fe-S(Met) bond photodissociation, recombination occurs on a thermally hot five-coordinate ground state.(*19*) In this study, we correlate the temperature decay of the hot ground state with Met rebinding to determine the enthalpy and entropy of the $Fe^{II}$-S(Met) bond. Both ferrous and ferric cyt *c* exhibits a red-shift in the oxidation state marker band $\nu_4$ following heme photoexcitation in $TR^3$ measurements.(*19*) It was shown that this band does not shift due to changes in spin state or loss of the Met ligand, and therefore this shift in frequency is interpreted as local heating in the heme active site;(*19*) shifts in Raman bands to lower frequency are consistent with an increase in sample temperature. Asher and Murtaugh measured the frequency shift in the $\nu_{10}$ core marker band of Ni octaethylporphyrin upon increased temperature(*30*). The temperature dependence of the $\nu_{10}$ band was modeled by including anharmonic coupling to a thermally populated low-frequency vibrational mode, as demonstrated by Harris et al.(*45*) Petrich et al demonstrated that this method could be applied to time-resolved resonance Raman measurements by applying this analysis to photoexcited carbonmonoxyhemoglobin.(*46*) They photoexcited carbonmonoxhemoglobin using a 575 nm optical pulse, forming deoxyhemoglobin. They then calculated the temperature of the heme using the following equation:

$$\Delta T(t) = \frac{-E_i/k}{\ln[\frac{\Delta\nu_t}{M}+\exp(-E_i/kT]} - T \quad (2)$$

where $E_i$ is the activation energy (which corresponds to the frequency of the low-frequency vibrational mode), $M$ reflects the strength of the anharmonic coupling between the low and high-frequency vibrational modes, and $\Delta\nu_t$ is the difference in frequency from the photoproduct. The values of $E_i$ and $M$ determined for the NiOEP $\nu_{10}$ band (528 $cm^{-1}$ and -73 $cm^{-1}$, respectively) were used for the hemoglobin $\nu_4$ and were shown to give reasonable results. Therefore, we have used the same method here to determine the increase in temperature of cyt *c* upon photoexcitation.

Fig. 9A of Ref. (*19*) displays the shift in frequency of the $\nu_4$ band as a function of time following photoexcitation. The steady-state frequency of 1360 $cm^{-1}$ steadily red-shifts to 1345 $cm^{-1}$ after ~1-2 ps; at this time, IVR is considered to be complete, resulting in a heme with an equilibrated, Boltzmann temperature; the frequency then shifts to higher energy in an approximately

exponential (i.e. unimolecular) process, eventually approaching the limit of 1353 $cm^{-1}$. The shift from 1345-1353 $cm^{-1}$ is interpreted as an indicator of temperature decay, and the $\Delta v_4$ values are used to obtain the temperature using the relationship from Ref. (*30*). The temperature values over the course of the Met rebinding vary from 456-320 K, which is within the range over which Asher and Murtaugh demonstrated that this method can be applied.

Because the system reaches thermal equilibrium after ~2 ps, we treat the cyt *c* ligand rebinding as an equilibrium process:

$$CytC + Met \Leftrightarrow CytC - Met \quad (3)$$

where the relative ratios of five-coordinate and six-coordinate cyt *c* heme sites are determined by the relative amounts of singlet and quintet species, as measured by Kβ-XES (*vide supra*). The excitation fraction was determined from the fits as 0.72. Because of the strong absorption of the solution, we expect inhomogeneous excitation through the jet, with a larger excitation fraction in front of the jet than in the back. The x-ray emission spectrum represents an ensemble average of the sample that is photoexcited and the sample that is not photoexcited. To remove the non-photoexcited sample from the thermodynamics analysis, the quintet species was normalized by the excitation fraction, and the singlet species was 1 – [quintet] (no intermediate is included at longer delay times.) Therefore,

$$K_{eq} = \frac{[CytC - Met]}{[CytC + Met]} = \frac{[Singlet]}{[Quintet]} \quad (4)$$

These values, with the temperature values, were used to generate the linear Van't Hoff plot shown in Fig. 3c. The slope of this plot equals ΔH/R, while the y-intercept equals -ΔS/R; therefore the slope and y-intercept of 3410.2 and -8.558 equate to a ΔH and ΔS of ~6.5 ± 1.2 kcal/mol and ~16.0 ± 3.2 cal/(mol*K), respectively. The error bars on the x-axis in Fig. 3c were determined using an error of ± 1 $cm^{-1}$ from the transient resonance Raman study, while the y-axis error bars assume a ± 5 % error in the singlet and quintet states from the XES analysis. The linear fit was not weighted to these individual errors.

**S.2 MXAN Simulations**

The structure of ground and excited-state cyt *c* were extracted from our Fe K-edge XAS data by generating DFT models with S=0 and S=2, respectively, and simulating the XAS spectrum using MXAN(*26*, *27*). The DFT model used for the ground-state was chosen because it adequately reproduced the covalency values determined in the cyt c RIXS measurement, as well as all of the metal vibrational modes observed in nuclear resonance vibrational spectroscopy (unpublished.) The best simulations for the ground and excited states are shown in Fig. 1c,d as determined by the resulting $\chi^2$ value. $\chi^2$ is calculated according to the method of Benfatto and Della-Longa (*26*):

$$\chi^2 = n * \sum_{i=1}^{m} [(y_i^{th} - y_i^{exp})\varepsilon_i^{-1}]^2 \quad (5)$$

where *m* is the number of data points, *n* is the number of independent points, $y^{th}$ and $y^{exp}$ are the simulated and experimental absorption values, respectively, and $\varepsilon$ is the individual error in the data set.

***S.2.1 Alternative Ground-State MXAN Simulations.***

The optimal simulation of the **GS** spectrum is shown in Fig. 1c. This simulation invoked a DFT structure where the geometry was optimized with the Fe-S(Met) bond distance fixed to its

EXAFS value of 2.29 Å.(*9*) DFT tends to overestimate this Fe-S distance, so an additional simulation was performed where the Fe-S(Met) bond distance was allowed to vary from the EXAFS distance in the DFT calculation (Fig. S2); the resulting structure was used to simulate the **GS** spectrum. The $\chi^2$ value of 3.3 was much higher than that obtained when the Fe(II)-S(Met) distance was fixed ($\chi^2$ = 2.4), indicating that the EXAFS distance is a better match to our data than the DFT distance in the **GS** spectrum. In particular, the simulation with the longer Fe-S(Met) bond distance poorly replicates the spectral feature ~30 eV past the edge, while this feature is reproduced adequately when the Fe-S(Met) distance is fixed to the EXAFS bond distance of 2.29 Å. In Fig. S3 this simulation is compared to the simulation from Fig. 1c.

***S.2.2 Alternative Excited-State MXAN Simulations.***

A series of MXAN simulations from DFT spectra were utilized to determine the cyt *c* heme **ES** structure. As a control, an MXAN simulation was performed using the **GS** structure to model the **ES** spectrum to demonstrate the sensitivity of MXAN to the structural changes between **GS** and **ES** (Fig. S4.) The optimal **ES** fit (Fig. 1d) allowed both the Fe-S(Met) and Fe-N(His) bond distances to vary in the DFT calculation, resulting in final bond distances of 3.04 and 2.15 Å, respectively. Subsequent DFT calculations and MXAN simulations were performed where the Fe-N(His) bond distance was fixed at various bond lengths to imitate Fe-N(His) bond photolysis in the excited state (Fig. S5,S6). The fixed bond distances are indicated in the figure captions. The $\chi^2$ values obtained from these simulations are worse than the $\chi^2$ of 1.9 obtained for the high-spin DFT model shown in Fig 1d. The residuals in Fig. S5 and S6 demonstrate that these simulations poorly reproduce the peak on the rising edge, as well as the two peaks at the top of the edge, and as such these structural models can be disregarded as proper models of the cyt *c* excited state.

***S.2.3 Met Distance Simulations***

Fig. S5 and S6 demonstrate that photoexcited cyt *c* does not exhibit N(His) bond photolysis. While the MXAN simulation of the high-spin DFT model shown in Fig. 1d does reproduce the XAS quite well, this does not reveal the sensitivity of the XAS to the Fe-S(Met) bond distance. A series of MXAN simulations were performed where the Fe-S(Met) distance of this model was varied to determine the sensitivity of these simulations to this scattering distance. The plot of the MXAN simulation $\chi^2$ as a function of the Fe-S(Met) distance in Fig. S7 indicates that the $\chi^2$ decreases with increasing Fe-S(Met) distance from 2.29 to ~3.04 Å, and then remains fairly consistent at larger distances. Therefore, our MXAN simulations indicate that the Fe-S(Met) distance is ≥ 3.04 Å.

***S.2.4 Individual Met Distance Simulations***

The MXAN simulations for Fe-S(Met) distances of 2.29, 2.44, 3.04, and 3.49 Å are shown in Fig. S8, along with overlaid plots of the experiment – simulation residual for these simulations. It should be noted that in the shape resonance region at higher energies the residuals for each of these simulations is quite similar, indicating that the shape resonance region rather insensitive to the Fe-S(Met) bond distance. Instead, this region is likely more sensitive to the other cyt *c* active site conformational changes, such as heme doming and core expansion. The residuals indicate significant differences in the rising edge and edge region; in particular, the simulations with shorter Fe-S(Met) distances exhibit larger residuals in the -2 to 0 eV range, indicating a poor match to the edge peak in these simulations. The XANES sensitivity to the Fe-S(Met)

distance in photoexcited cyt *c* is exhibited most in the edge region, and we confirm a Fe-S(Met) distance ≥ 3 Å due to the better match (lower residuals) in the first ~ 20 eV of the XANES.

## S.3 Laser Power Controls

### *S.3.1 Laser Power Titration*

A high laser fluence, such as that utilized in this study (20 mJ/cm$^2$, ~3 photons/heme), can result in multi-photon absorption effects and distortion of the excited-state dynamics. In order to avoid multi-photon absorption, a power titration scan was performed where the change in the Kβ-XES was measured as a function of the laser fluence. This measurement was performed at 600 fs time delay to ensure that a large excited-state change in the spectrum was observed. The power titration scan is shown in Fig. S12, where the integrated emission signal over the energy range of 7049-7059 eV is plotted as a function of laser fluence. The plot is expected to be linear so long as each individual molecule absorbs only one photon. The power titration is linear from 1 – 20 mJ/cm$^2$; exciting with a laser fluence in this range will yield a high excitation fraction while minimizing multi-photon absorption effects.

### *S.3.2 Thermodynamics Analysis Using Ultrafast Optical Transient Absorption*

Optical transient absorption measurements utilized much lower laser fluences in the excitation pulse. As an additional control, we determine the $K_{eq}$ values from optical transient absorption (TA) measurements and perform the same thermodynamics analysis shown in Fig. 3c. The determination of the quintet and singlet populations, as well as the corresponding Van't Hoff plot, are shown in Fig. S13. The transient absorption spectrum is shown in Fig. S13a, following noise reduction by singular value decomposition, as well as removal of laser pump scatter. At each time delay, the absolute value of the signal was summed along the wavelength axis and the resulting decay curve was assumed to be proportional to the quintet population after ~600 fs. The excitation fraction could not be determined from the TA data and instead was determined by solving the rate equation using both the laser (temporal width, fluence, etc.) and sample (concentration, path length) parameters, yielding an excitation fraction of ~10 %. Because the maximum difference signal is observed at 600 fs in the TA, this time point of the summed TA signal was scaled to 10 % quintet state. The resulting time evolution of the quintet population is shown in Fig. S13b; also shown are the calculated values from the rate equation, determined using the excitation fraction and assuming exponential decay. The quintet and singlet values for the thermodynamic analysis were then determined using the same method employed in the XES, by taking the quintet values at times matching the time-resolved resonance Raman data and scaling by the excitation fraction. The resulting Van't Hoff plot is shown in Fig. S13c. The ΔH and ΔS values determined in this way are consistent with those determined by the XES analysis. Because the pump laser fluence in the TA measurement is much lower than the XES (~0.85 vs. 20 mJ/cm$^2$), we conclude that the ΔH and ΔS values are not affected by multi-photon absorption. For the TA analysis, it is unclear how much error is present in the $K_{eq}$ values.

## S.4 X-ray Absorption Time Dependence

Due to the large data acquisition time required for collecting the ultrafast XAS, the full spectrum was only collected at a single time delay (600 fs). In order to observe time-dependent structural dynamics, we instead performed time scans at several energies where the difference

between the ground and photoexcited spectra was largest. The energies collected were 7128, 7136, 7147, and 7203 eV, shown in Fig. S14. Each of these time scans can be fit with a single exponential with a 5 to 8 ps time constant, consistent with the monoexponential kinetics exhibited in the XES. In order to improve the quality of the XAS time scans, the scans from each energy were rescaled such that all the time scans from all energies was overlaid and averaged. This new time scan is plotted with the XES in Fig. S15. We observe that the XAS kinetics match the XES quite well, indicating that there is not significant structural evolution in this system; the change in the spectrum over time instead reflects a conversion from five-coordinate, Met-off to six-coordinate, Met-bound.

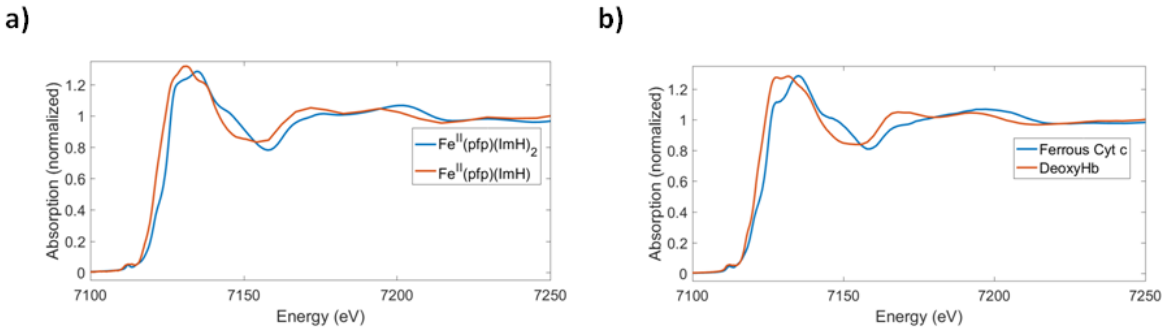


**Fig. S1 – Ground-State XAS Reference Spectra.** Fe K-edge XAS reference spectra of six-coordinate, low-spin (blue) and five-coordinate, high-spin (red) hemes; a) ferrous heme model complexes, where pfp = picket-fence porphyrin and ImH = imidazole; b) ferrous heme proteins, where deoxyHb = deoxyhemoglobin

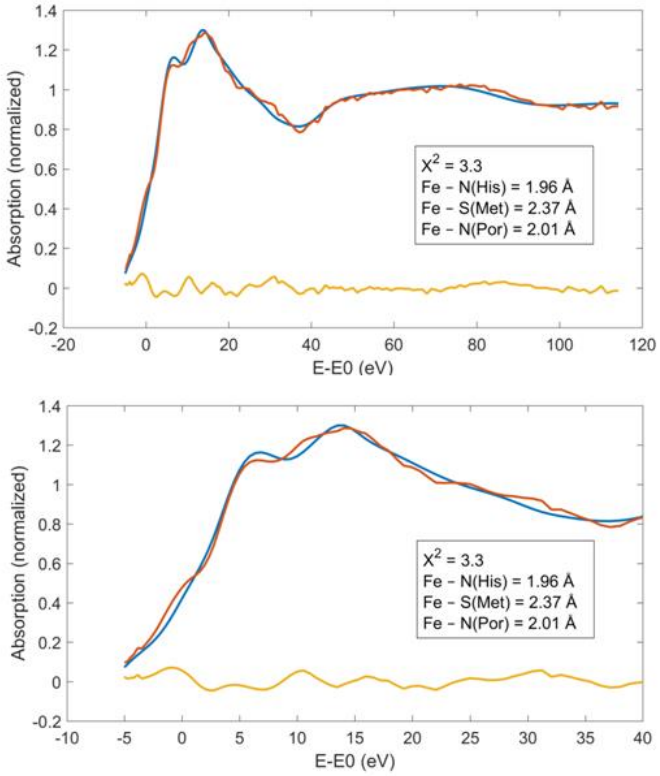


**Fig. S2 – Ground-State XAS Simulation With Floating Met.** Red: Experimental ground-state cyt c spectrum; Blue: MXAN simulation of the ground-state cyt *c* spectrum where the Fe-S(Met) bond distance is allowed to optimize from the EXAFS distance of 2.29 Å; Yellow: Residual of fit (experiment - simulation.) The top plot shows the full energy range, while the bottom plot focuses on the edge and excludes the shape resonances.

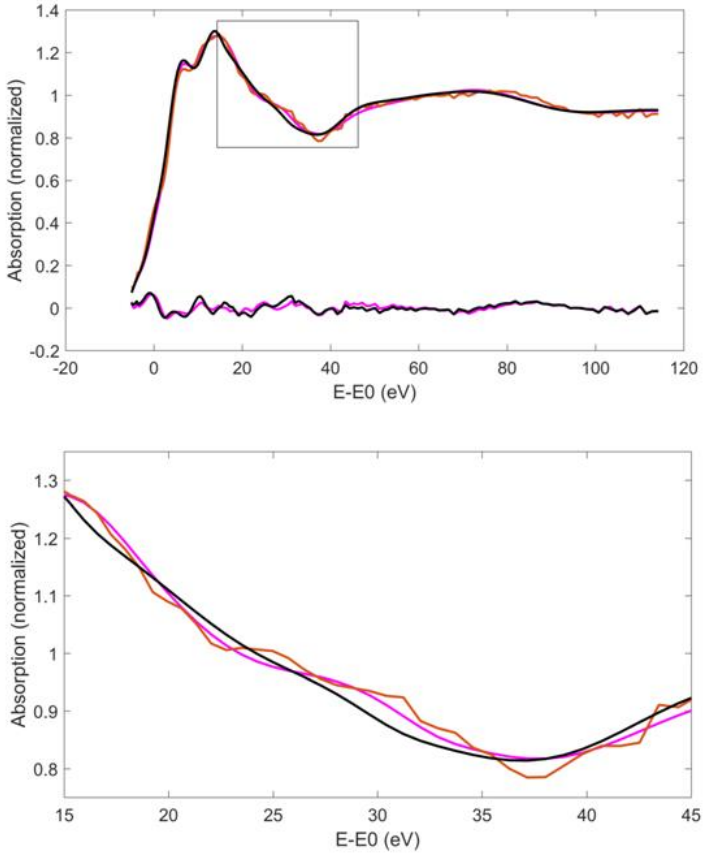


**Fig. S3 – Comparison of Ground-State MXAN Simulations.** Red: Experimental ground-state cyt *c* spectrum; Black: MXAN simulation of the ground-state cyt *c* spectrum where the Fe-S(Met) bond distance is 2.37 Å (DFT optimized value); Purple: MXAN simulation of the ground-state cyt *c* spectrum where the Fe-S(Met) bond distance is 2.29 Å (EXAFS value). The top plot shows the full energy range, while the bottom plot zooms on the boxed region of the top plot. The simulation for an Fe-S(Met) distance of 2.29 Å better reproduces the experimental spectrum ($\chi^2$ of 2.4 vs. 3.3.) Of particular note is the spectral feature ~30 eV past the edge, which is replicated well when the EXAFS distance is used, but is poorly replicated when using the DFT distance.

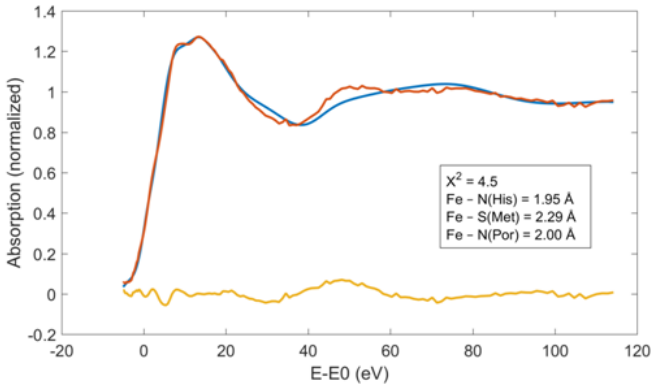


**Fig. S4 – Excited-State XAS Simulation Using Ground-State Structure.** Red: Experimental excited-state cyt *c* spectrum; Blue: MXAN simulation of the excited-state cyt *c* spectrum using the ground-state cyt *c* structure (structure used in Fig. 1c); Yellow: Residual of fit (experiment - simulation.) Very large $\chi^2$ indicates a very poor fit. Particularly poor fit in the range of 15 – 60 eV.

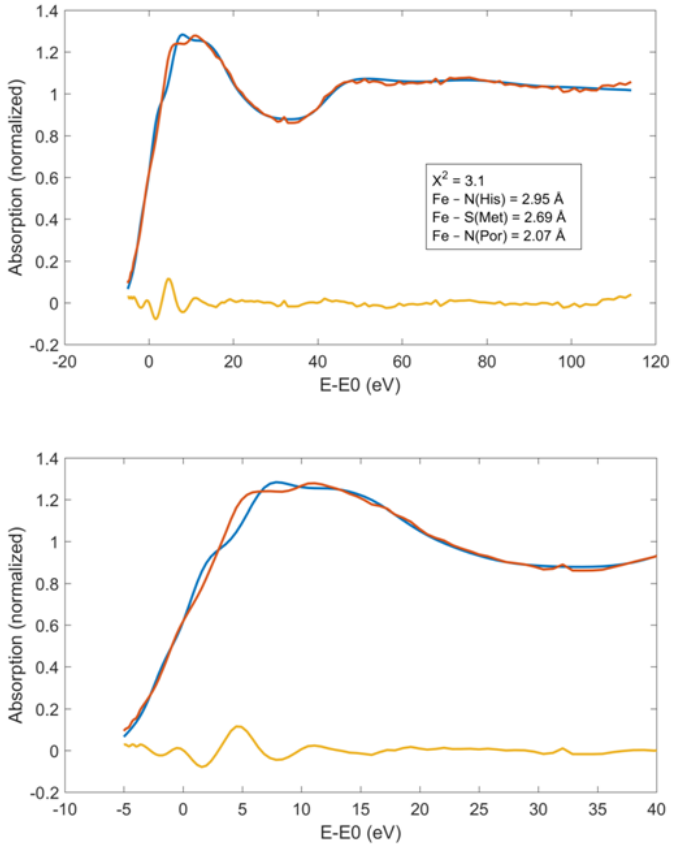


**Fig. S5 – Excited-State XAS Simulation With 2.95 Å His Bond Length.** Red: Experimental excited-state cyt *c* spectrum; Blue: MXAN simulation of the excited-state cyt *c* spectrum with Fe-N(His) bond distance fixed to 2.95 Å; Yellow: Residual of fit (experiment - simulation.) Top plot shows the full energy range, while bottom plot focuses on the edge region. The fit in the edge region is particularly poor, as evidenced by the large residuals, and therefore this structural model can be dismissed as an accurate model of the excited state.

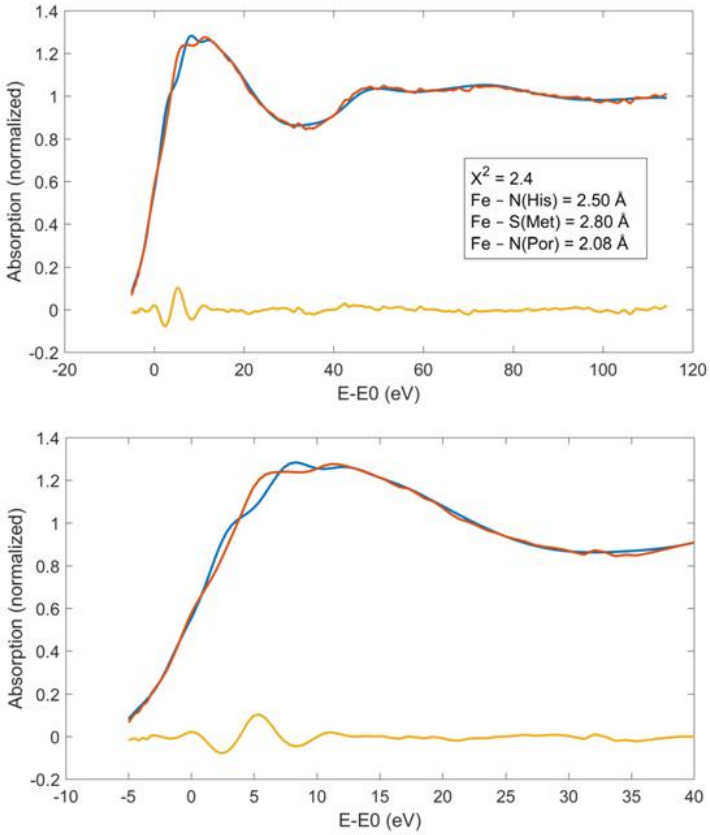


**Fig. S6 – Excited-State XAS Simulation With 2.50 Å His Bond Length.** Red: Experimental excited-state cyt *c* spectrum; Blue: MXAN simulation of the excited-state cyt *c* spectrum with Fe-N(His) bond distance fixed to 2.50 Å; Yellow: Residual of fit (experiment - simulation.) Top plot shows the full energy range, while bottom plot focuses on the edge region. As with the previous simulation, the simulated spectrum matches the experimental spectrum rather poorly in the edge region.

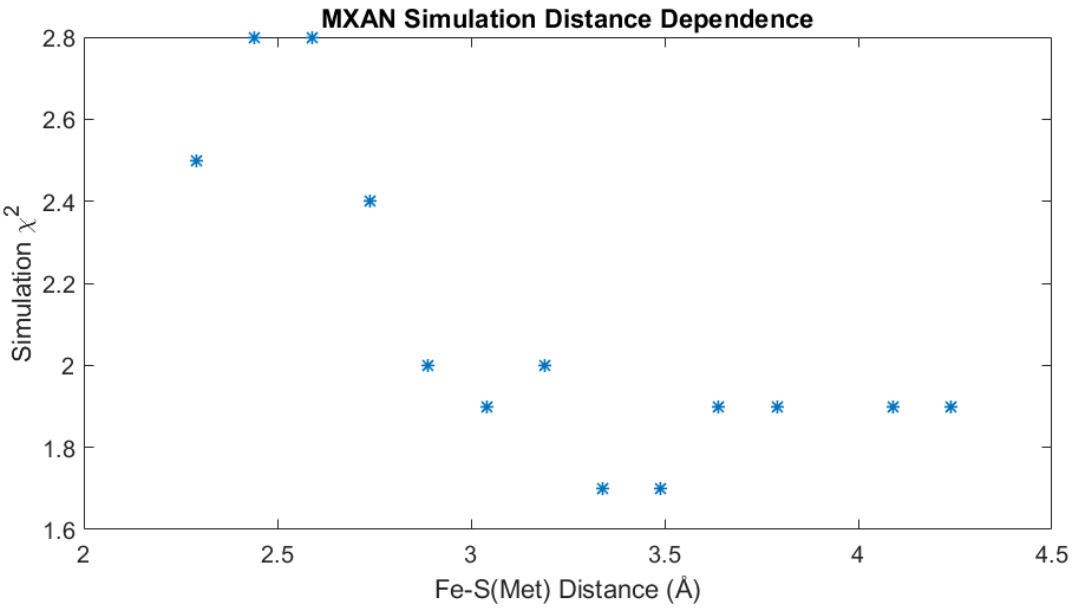


**Fig. S7 – Fe-S(Met) Distance Dependence in MXAN Simulations.** The high-spin model used in Fig. 1d was taken, and the Fe-S(Met) distance varied from 2.29 to 4.24 Å. The MXAN simulation $\chi^2$ for these simulations is plotted as a function of the Fe-S(Met) distance. Generally, $\chi^2$ drops with increasing Fe-S(Met) distance until ~2.9 Å, where the $\chi^2$ levels out. These simulations show that the Fe-S(Met) distance in photoexcited cyt c is ≥ 2.9 Å.

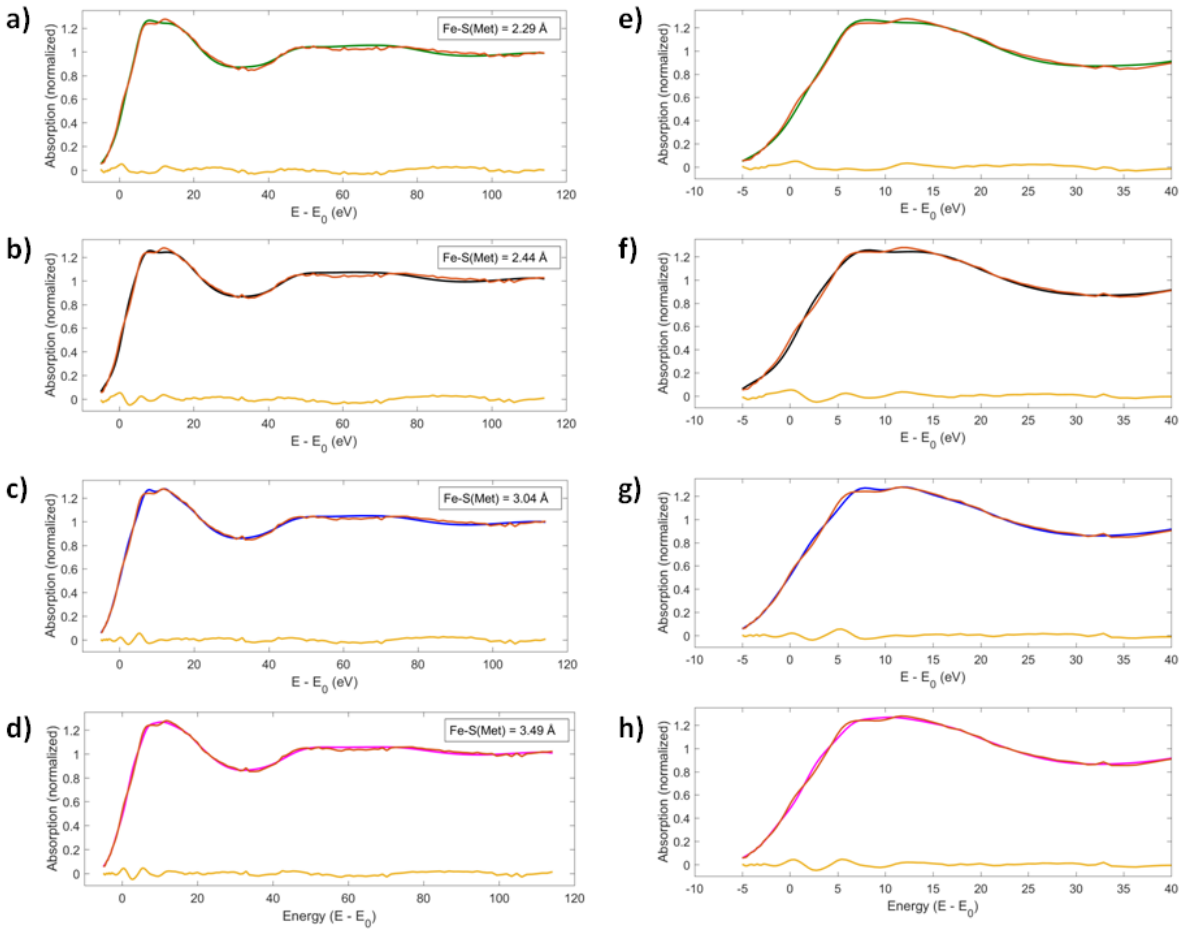
a)
Fe-S(Met) = 2.29 Å
b)
Fe-S(Met) = 2.44 Å
c)
Fe-S(Met) = 3.04 Å
d)
Fe-S(Met) = 3.49 Å
e)
f)
g)
h)
Absorption (normalized)
E - E0 (eV)
Energy (E - E0)

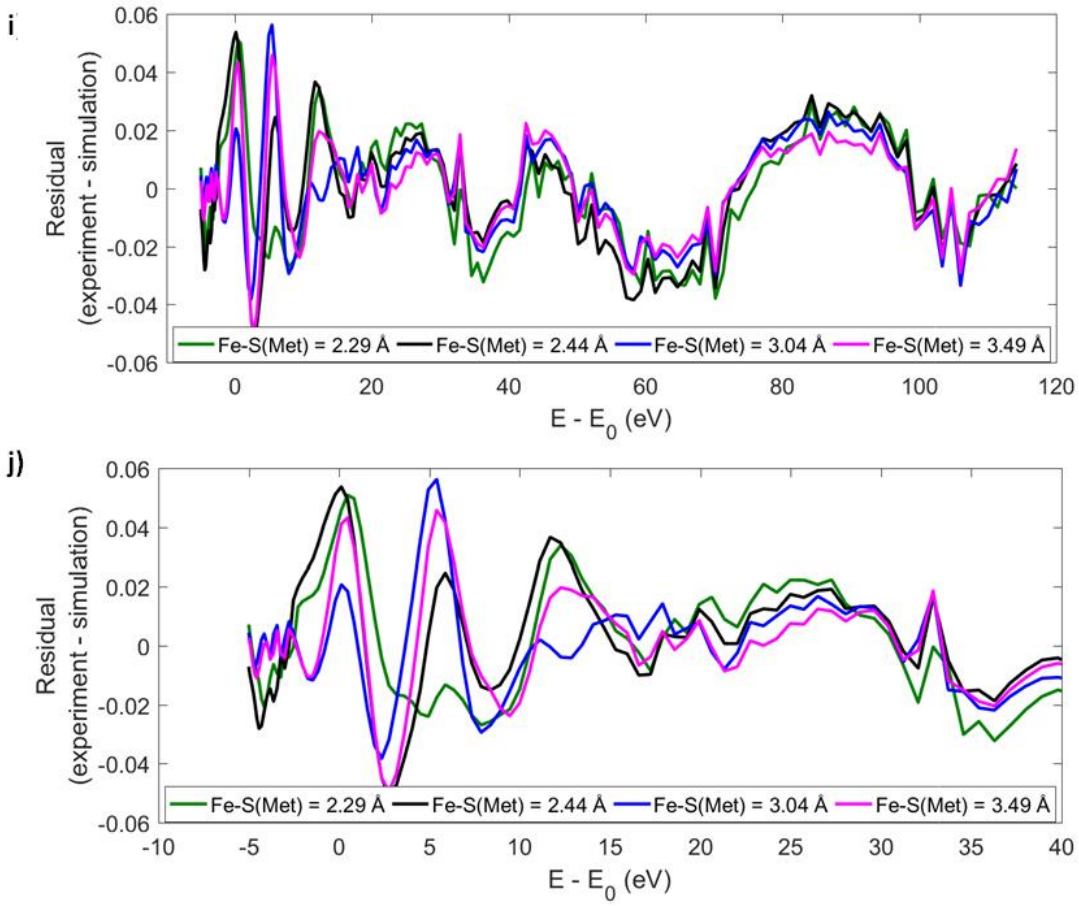


**Fig. S8 – Fe-S(Met) Distance Dependence in MXAN Simulations.** Select MXAN simulations from the Fe-S(Met) distance dependence shown in Fig. S9. The full energy range of the MXAN simulations for Fe-S(Met) distances of a) 2.29 Å, b) 2.44 Å, c) 3.04 Å, and d) 3.49 Å. A zoomed in plot of the edge region for e) 2.29 Å, f) 2.44 Å, g) 3.04 Å, and h) 3.49 Å are also shown. The residuals for each of these four simulations are also plotted separately displaying the full (i) and edge (j) energy ranges. The residual plots show that variation of the Fe-S(Met) distance has generally minor effects on the shape resonance at energies > ~20 eV. The primary differences are observed in the rising edge and edge peak regions encompassing the first ~ 20 eV of the XAS. The simulations at smaller Fe-S(Met) distances, i.e. the 2.29 (green) and 2.44 (black) Å simulations have a particularly poor match to the edge peak, resulting in large residuals from -2 to 0 eV, while the longer time distances of 3.04 (blue) and 3.49 (purple) Å show smaller residuals both on the rising edge and throughout the edge region.

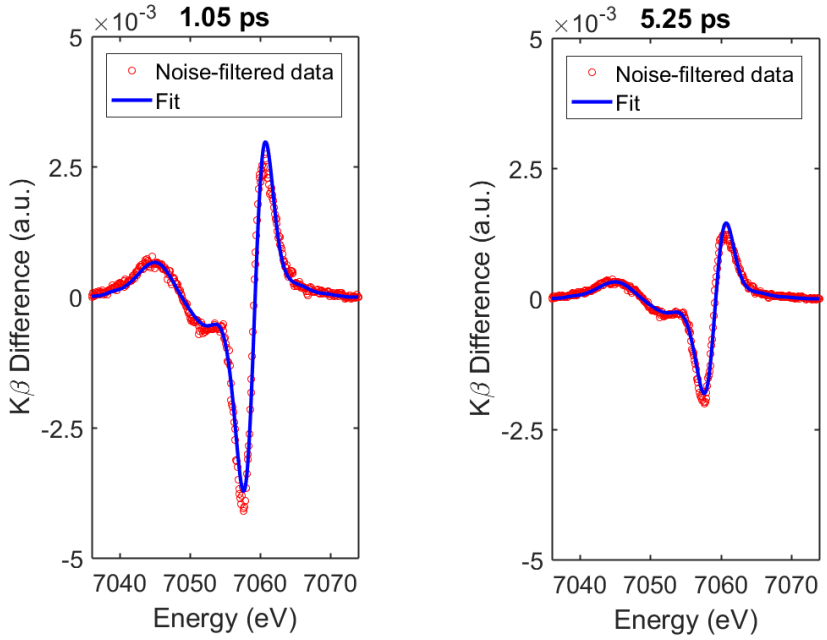


**Fig. S9 – Modeling of Kβ XES Difference Spectra.** Fit of the noise-filtered transients at pump-probe delays of a) 1.05 ps and b) 5.25 ps using the quintet-singlet difference spectrum. The difference spectrum was broadened to account for misalignment in the XES spectrometer.

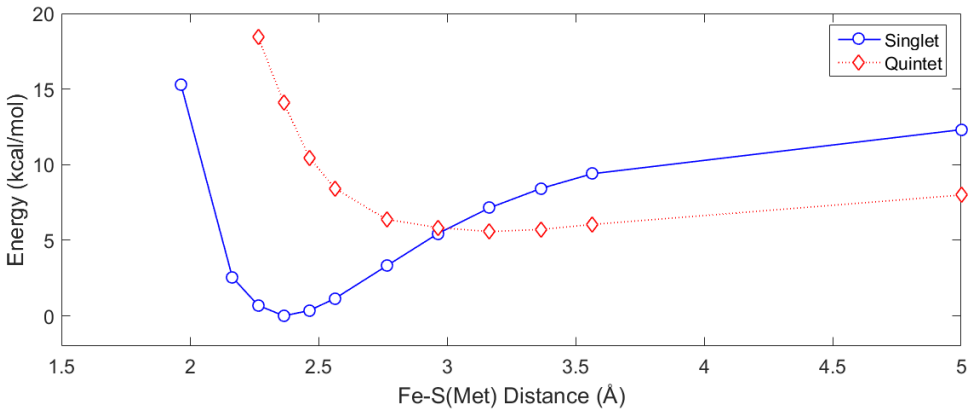


**Fig. S10 – Cyt *c* Singlet and Quintet Potential Energy Surfaces.** Potential energy surfaces for the singlet and quintet species with variation of the Fe-S(Met) bond distance. Calculations parallel those performed in Ref. (*14*). The singlet and quintet states spin-orbit couple at the crossing point via a $^3T_1$ state.

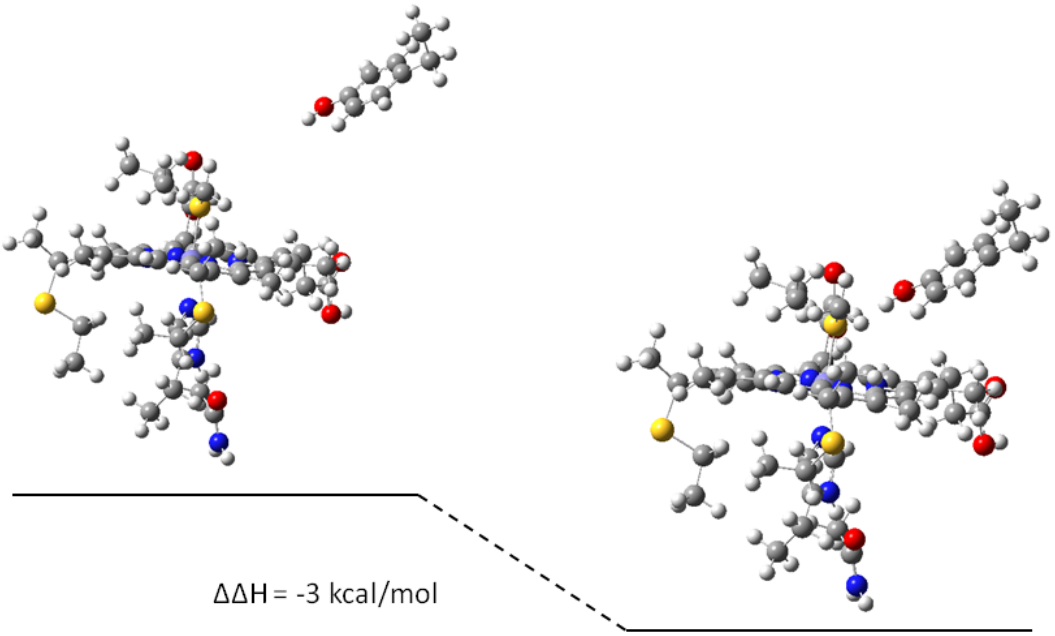


**Fig. S11 – Calculated Hydrogen Bonding Stabilization.** DFT calculation of Tyr-OH---S(Met) hydrogen bond strength; ΔH determined from frequency calculations; DFT calculations performed as described in Materials and Methods section.

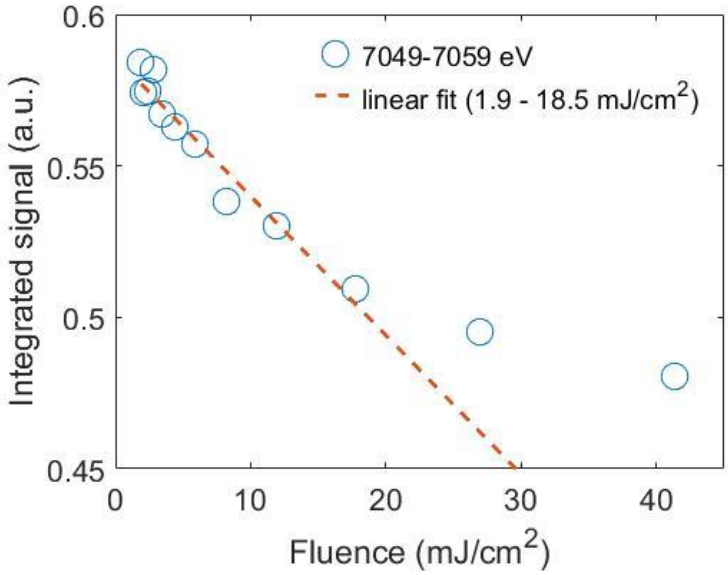


**Fig. S12 – Laser Power Titration.** Plot of the integrated emission signal (from 7049 to 7059 eV) vs. the optical pump laser fluence. The fit is linear over the range of 0 to 20 mJ/cm$^2$, and therefore minimal two-photon absorption is expected over this fluence range.

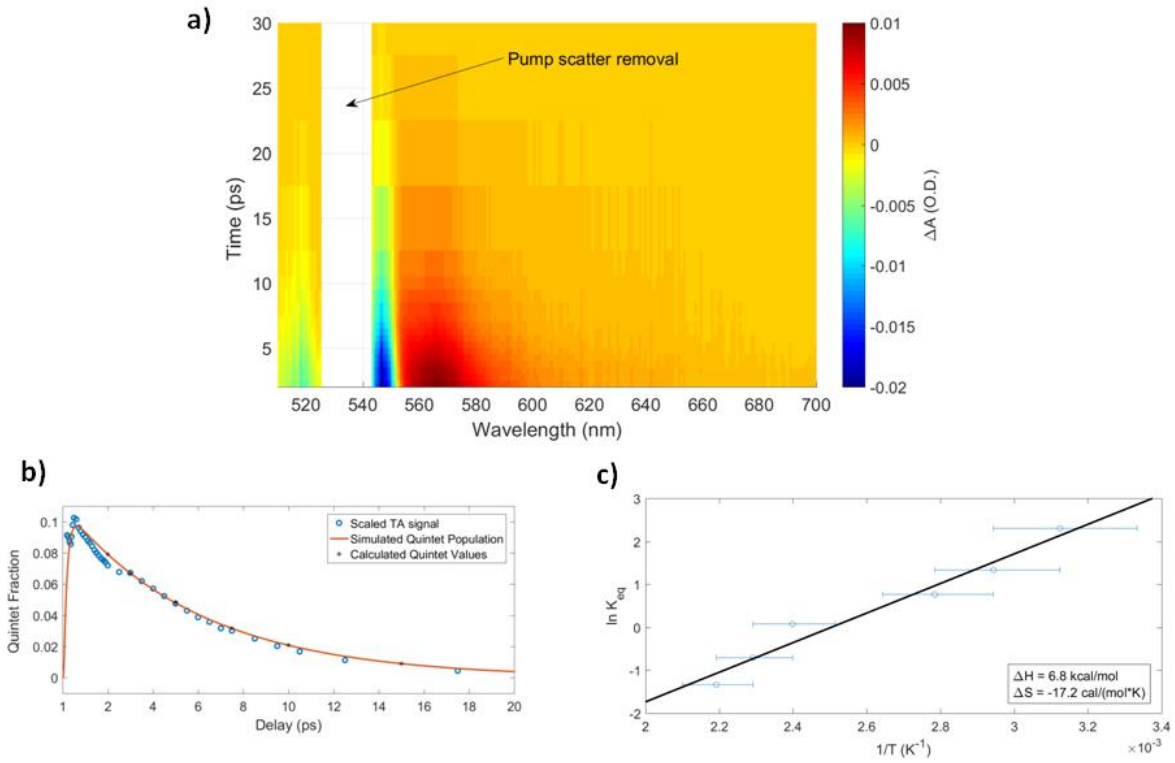


**Fig. S13 – Thermodynamics from Optical Transient Absorption.** The Fe-S(Met) ΔH and ΔS were determined from TA for comparison with the values from XES analysis. a) TA spectrum plotted as a function of time and wavelength; note that the portion of the spectrum affected by laser pump scatter was removed from the analysis, and noise was filtered by SVD analysis. b) Plot of quintet fraction over time; the excitation fraction was estimated by solving the rate equation using laser and sample parameters; the integrated TA signal (blue) was scaled by the excitation fraction, with 600 fs set to 10% quintet population, as this was when the maximum TA signal was observed; the simulated quintet population (red) is from the results of the rate equation, assuming a 6.1 ps decay. c) Van't Hoff plot using TA quintet and singlet populations. The ΔH and ΔS from the fit are consistent with those from the XES analysis; because the optical TA is performed with low laser fluence (~ 0.8 mJ/cm$^2$), the XES analysis is shown to exhibit no measurable effects from multi-photon absorption.

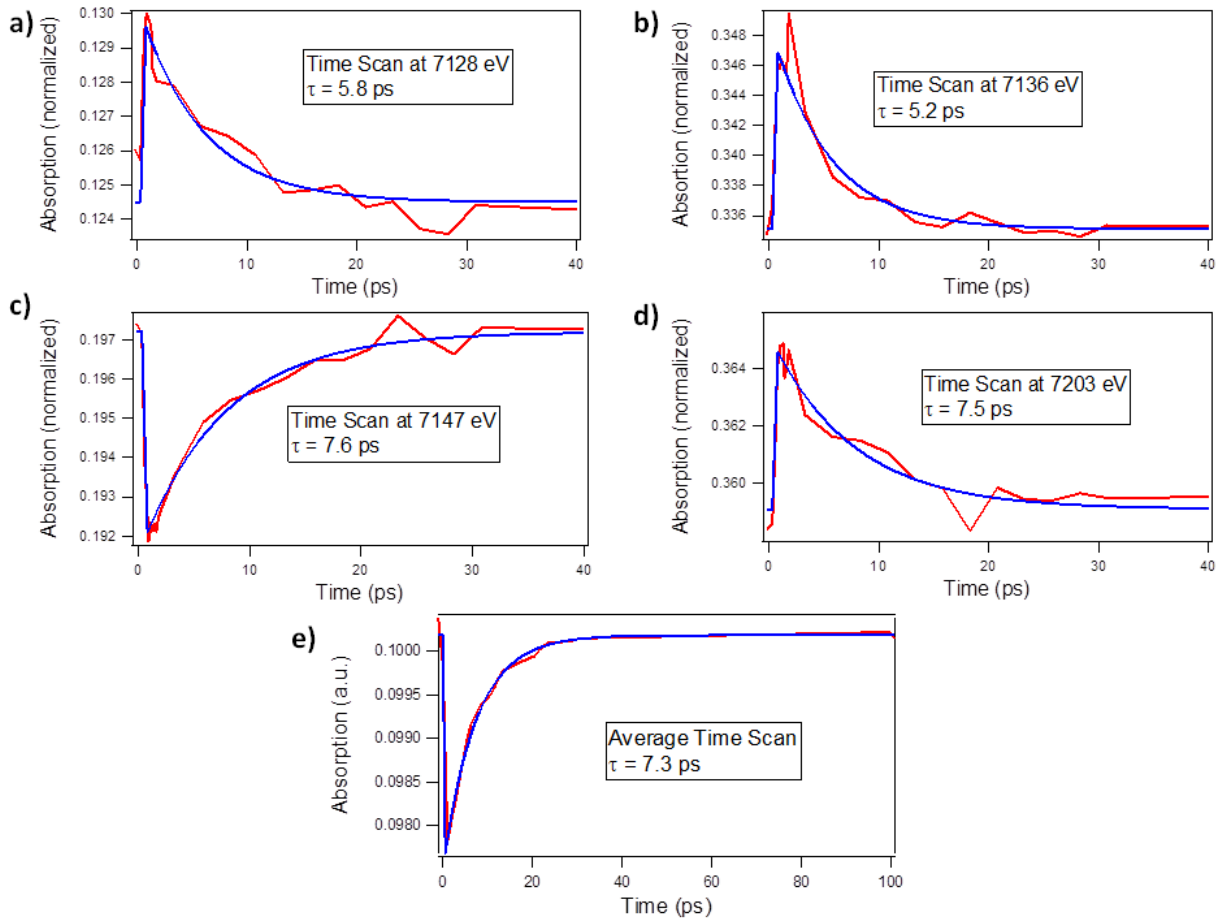


**Fig. S14 – XAS Time Scans.** XAS time delay scans at a) 7128 eV, b) 7136 eV, c) 7147 eV, and d) 7203 eV. All of these time scans exhibit exponential decay with τ = 5 to 8 ps, consistent with optical transient absorption and XES results; e) average of all time scans, where each scan was rescaled to allow for proper averaging. The average time scan also exhibits an exponential decay consistent with optical transient absorption and XES measurements.

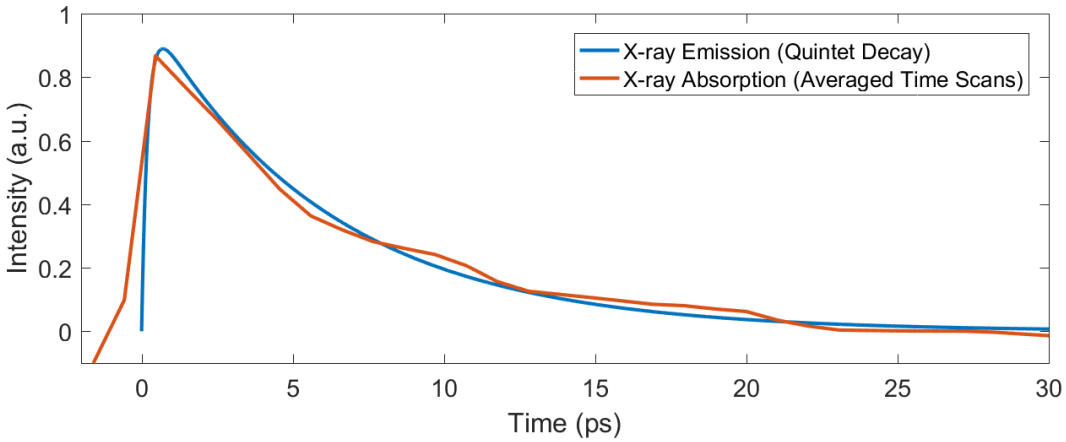


**Fig. S15 – Comparison of XAS and XES Time Decay.** Comparison of the time decay exhibited by the XES (blue) and XAS (red) data. Spectra overlay quite well within the noise, indicating that the dynamics in the XAS spectra match those in the XES spectra.

**References and Notes**


1. R. A. Scott, A. G. Mauk, *Cytochrome C: A Multidisciplinary Approach* (University Science Books, 1996).

2. G. W. Pettigrew, G. R. Moore, *Cytochromes c: Biological Aspects* (Springer-Verlag, 1987).

3. J. Liu, S. Chakraborty, P. Hosseinzadeh, Y. Yu, S. Tian, I. Petrik, A. Bhagi, Y. Lu, Metalloproteins containing cytochrome, iron-sulfur, or copper redox centers. *Chem. Rev.* **114**, 4366–4469 (2014). doi:10.1021/cr400479b Medline

4. S. Ghosh, X. Xie, A. Dey, Y. Sun, C. P. Scholes, E. I. Solomon, Thermodynamic equilibrium between blue and green copper sites and the role of the protein in controlling function. *Proc. Natl. Acad. Sci. U.S.A.* **106**, 4969–4974 (2009). doi:10.1073/pnas.0900995106 Medline

5. H. B. Gray, B. G. Malmström, R. J. P. Williams, Copper coordination in blue proteins. *J. Biol. Inorg. Chem.* **5**, 551–559 (2000). doi:10.1007/s007750000146 Medline

6. M.-L. Tsai, R. G. Hadt, N. M. Marshall, T. D. Wilson, Y. Lu, E. I. Solomon, Axial interactions in the mixed-valent CuA active site and role of the axial methionine in electron transfer. *Proc. Natl. Acad. Sci. U.S.A.* **110**, 14658–14663 (2013). doi:10.1073/pnas.1314242110 Medline

7. V. E. Kagan, V. A. Tyurin, J. Jiang, Y. Y. Tyurina, V. B. Ritov, A. A. Amoscato, A. N. Osipov, N. A. Belikova, A. A. Kapralov, V. Kini, I. I. Vlasova, Q. Zhao, M. Zou, P. Di, D. A. Svistunenko, I. V. Kurnikov, G. G. Borisenko, Cytochrome c acts as a cardiolipin oxygenase required for release of proapoptotic factors. *Nat. Chem. Biol.* **1**, 223–232 (2005). doi:10.1038/nchembio727 Medline

8. Y. P. Ow, D. R. Green, Z. Hao, T. W. Mak, Cytochrome c: Functions beyond respiration. *Nat. Rev. Mol. Cell Biol.* **9**, 532–542 (2008). doi:10.1038/nrm2434 Medline

9. M.-C. Cheng, A. M. Rich, R. S. Armstrong, P. J. Ellis, P. A. Lay, Determination of iron−ligand bond lengths in ferric and ferrous horse heart cytochrome c using multiple-scattering analyses of XAFS data. *Inorg. Chem.* **38**, 5703–5708 (1999). doi:10.1021/ic990395r

10. F. A. Tezcan, J. R. Winkler, H. B. Gray, Effects of ligation and folding on reduction potentials of heme proteins. *J. Am. Chem. Soc.* **120**, 13383–13388 (1998). doi:10.1021/ja982536e

11. G. R. Moore, R. J. P. Williams, Nuclear-magnetic-resonance studies of ferrocytochrome c. pH and temperature dependence. *Eur. J. Biochem.* **103**, 513–521 (1980). doi:10.1111/j.1432-1033.1980.tb05975.x Medline

12. G. R. Moore, R. J. P. Williams, The stability of ferricytochrome c. Temperature dependence of its NMR spectrum. *Eur. J. Biochem.* **103**, 523–532 (1980). doi:10.1111/j.1432-1033.1980.tb05976.x Medline

13. A. L. Raphael, H. B. Gray, Axial ligand replacement in horse heart cytochrome c by semisynthesis. *Proteins* **6**, 338–340 (1989). doi:10.1002/prot.340060316 Medline

14. T. Kroll, R. G. Hadt, S. A. Wilson, M. Lundberg, J. J. Yan, T.-C. Weng, D. Sokaras, R. Alonso-Mori, D. Casa, M. H. Upton, B. Hedman, K. O. Hodgson, E. I. Solomon, Resonant inelastic X-ray scattering on ferrous and ferric bis-imidazole porphyrin and cytochrome c: Nature and role of the axial methionine-Fe bond. *J. Am. Chem. Soc.* **136**, 18087–18099 (2014). doi:10.1021/ja5100367 Medline

15. E. I. Solomon, R. G. Hadt, Recent advances in understanding blue copper proteins. *Coord. Chem. Rev.* **255**, 774–789 (2011). doi:10.1016/j.ccr.2010.12.008

16. E. I. Solomon, R. K. Szilagyi, S. DeBeer George, L. Basumallick, Electronic structures of metal sites in proteins and models: Contributions to function in blue copper proteins. *Chem. Rev.* **104**, 419–458 (2004). doi:10.1021/cr0206317 Medline

17. O. Bräm, C. Consani, A. Cannizzo, M. Chergui, Femtosecond UV studies of the electronic relaxation processes in cytochrome c. *J. Phys. Chem. B* **115**, 13723–13730 (2011). doi:10.1021/jp207615u Medline

18. W. Wang, X. Ye, A. A. Demidov, F. Rosca, T. Sjodin, W. X. Cao, M. Sheeran, P. M. Champion, Femtosecond multicolor pump−probe spectroscopy of ferrous cytochrome c. *J. Phys. Chem. B* **104**, 10789–10801 (2000). doi:10.1021/jp0008602

19. M. Negrerie, S. Cianetti, M. H. Vos, J.-L. Martin, S. G. Kruglik, Ultrafast heme dynamics in ferrous versus ferric cytochrome c studied by time-resolved resonance Raman and transient absorption spectroscopy. *J. Phys. Chem. B* **110**, 12766–12781 (2006). doi:10.1021/jp0559377 Medline

20. E. R. Henry, W. A. Eaton, R. M. Hochstrasser, Molecular dynamics simulations of cooling in laser-excited heme proteins. *Proc. Natl. Acad. Sci. U.S.A.* **83**, 8982–8986 (1986). doi:10.1073/pnas.83.23.8982 Medline

21. P. Li, P. M. Champion, Investigations of the thermal response of laser-excited biomolecules. *Biophys. J.* **66**, 430–436 (1994). doi:10.1016/S0006-3495(94)80793-3 Medline

22. Y. Zhang, J. E. Straub, Diversity of solvent dependent energy transfer pathways in heme proteins. *J. Phys. Chem. B* **113**, 825–830 (2009). doi:10.1021/jp807499y Medline

23. T. Kitagawa, T. G. Spiro, Eds., *Biological Applications of Raman Spectroscopy* (Wiley, 1988), vol. 3, pp. 97–131.

24. Ch. Bressler, C. Milne, V.-T. Pham, A. Elnahhas, R. M. van der Veen, W. Gawelda, S. Johnson, P. Beaud, D. Grolimund, M. Kaiser, C. N. Borca, G. Ingold, R. Abela, M. Chergui, Femtosecond XANES study of the light-induced spin crossover dynamics in an iron(II) complex. *Science* **323**, 489–492 (2009). doi:10.1126/science.1165733 Medline

25. W. Zhang, R. Alonso-Mori, U. Bergmann, C. Bressler, M. Chollet, A. Galler, W. Gawelda, R. G. Hadt, R. W. Hartsock, T. Kroll, K. S. Kjær, K. Kubiček, H. T. Lemke, H. W. Liang, D. A. Meyer, M. M. Nielsen, C. Purser, J. S. Robinson, E. I. Solomon, Z. Sun, D. Sokaras, T. B. van Driel, G. Vankó, T.-C. Weng, D. Zhu, K. J. Gaffney, Tracking excited-state charge and spin dynamics in iron coordination complexes. *Nature* **509**, 345–348 (2014). doi:10.1038/nature13252 Medline

26. M. Benfatto, S. Della Longa, Geometrical fitting of experimental XANES spectra by a full multiple-scattering procedure. *J. Synchrotron Radiat.* **8**, 1087–1094 (2001). doi:10.1107/S0909049501006422 Medline

27. M. Benfatto, S. D. Longa, P. D'Angelo, Advances in the theoretical analysis of the XANES (X-ray Absorption Near Edge Structure) energy region for quantitative structural use. *Phys. Scr.* **2005**, 28 (2005). doi:10.1238/Physica.Topical.115a00028

28. P. Glatzel, U. Bergmann, High resolution 1s core hole X-ray spectroscopy in 3d transition metal complexes—Electronic and structural information. *Coord. Chem. Rev.* **249**, 65–95 (2005). doi:10.1016/j.ccr.2004.04.011

29. H. S. Cho, N. Dashdorj, F. Schotte, T. Graber, R. Henning, P. Anfinrud, Protein structural dynamics in solution unveiled via 100-ps time-resolved x-ray scattering. *Proc. Natl. Acad. Sci. U.S.A.* **107**, 7281–7286 (2010). doi:10.1073/pnas.1002951107 Medline

30. S. A. Asher, J. Murtaugh, Metalloporphyrin gas and condensed-phase resonance Raman studies: The role of vibrational anharmonicities as determinants of Raman frequencies. *J. Am. Chem. Soc.* **105**, 7244–7251 (1983). doi:10.1021/ja00363a006

31. S. Zaidi, M. I. Hassan, A. Islam, F. Ahmad, The role of key residues in structure, function, and stability of cytochrome-c. *Cell. Mol. Life Sci.* **71**, 229–255 (2014). doi:10.1007/s00018-013-1341-1 Medline

32. D. L. Howard, H. G. Kjaergaard, Hydrogen bonding to divalent sulfur. *Phys. Chem. Chem. Phys.* **10**, 4113–4118 (2008). doi:10.1039/b806165c Medline

33. L. Serpas, B. Milorey, L. A. Pandiscia, A. W. Addison, R. Schweitzer-Stenner, Autoxidation of reduced horse heart cytochrome c catalyzed by cardiolipin-containing membranes. *J. Phys. Chem. B* **120**, 12219–12231 (2016). doi:10.1021/acs.jpcb.6b05620 Medline

34. E. K. J. Tuominen, C. J. A. Wallace, P. K. J. Kinnunen, Phospholipid-cytochrome c interaction: Evidence for the extended lipid anchorage. *J. Biol. Chem.* **277**, 8822–8826 (2002). doi:10.1074/jbc.M200056200 Medline

35. L. J. McClelland, H. B. B. Steele, F. G. Whitby, T.-C. Mou, D. Holley, J. B. A. Ross, S. R. Sprang, B. E. Bowler, Cytochrome c can form a well-defined binding pocket for hydrocarbons. *J. Am. Chem. Soc.* **138**, 16770–16778 (2016). doi:10.1021/jacs.6b10745 Medline

36. D. A. Capdevila, S. Oviedo Rouco, F. Tomasina, V. Tortora, V. Demicheli, R. Radi, D. H. Murgida, Active site structure and peroxidase activity of oxidatively modified cytochrome c species in complexes with cardiolipin. *Biochemistry* **54**, 7491–7504 (2015). doi:10.1021/acs.biochem.5b00922 Medline

37. L. A. Pandiscia, R. Schweitzer-Stenner, Coexistence of native-like and non-native cytochrome c on anionic liposomes with different cardiolipin content. *J. Phys. Chem. B* **119**, 12846–12859 (2015). doi:10.1021/acs.jpcb.5b07328 Medline

38. F. Zhang, E. S. Rowe, Calorimetric studies of the interactions of cytochrome c with dioleoylphosphatidylglycerol extruded vesicles: Ionic strength effects. *Biochim. Biophys. Acta* **1193**, 219–225 (1994). doi:10.1016/0005-2736(94)90156-2 Medline

39. J. Yoon, S. Fujii, E. I. Solomon, Geometric and electronic structure differences between the type 3 copper sites of the multicopper oxidases and hemocyanin/tyrosinase. *Proc. Natl. Acad. Sci. U.S.A.* **106**, 6585–6590 (2009). doi:10.1073/pnas.0902127106 Medline

40. B. E. R. Snyder, P. Vanelderen, M. L. Bols, S. D. Hallaert, L. H. Böttger, L. Ungur, K. Pierloot, R. A. Schoonheydt, B. F. Sels, E. I. Solomon, The active site of low-temperature methane hydroxylation in iron-containing zeolites. *Nature* **536**, 317–321 (2016). doi:10.1038/nature19059 Medline

41. M. Chollet, R. Alonso-Mori, M. Cammarata, D. Damiani, J. Defever, J. T. Delor, Y. Feng, J. M. Glownia, J. B. Langton, S. Nelson, K. Ramsey, A. Robert, M. Sikorski, S. Song, D. Stefanescu, V. Srinivasan, D. Zhu, H. T. Lemke, D. M. Fritz, The x-ray pump-probe instrument at the linac coherent light source. *J. Synchrotron Radiat.* **22**, 503–507 (2015). doi:10.1107/S1600577515005135 Medline

42. R. Alonso-Mori, J. Kern, D. Sokaras, T.-C. Weng, D. Nordlund, R. Tran, P. Montanez, J. Delor, V. K. Yachandra, J. Yano, U. Bergmann, A multi-crystal wavelength dispersive x-ray spectrometer. *Rev. Sci. Instrum.* **83**, 073114 (2012). doi:10.1063/1.4737630 Medline

43. A. Tenderholt, B. Hedman, K. O. Hodgson, PySpline: A Modern, Cross-platform program for the processing of raw averaged XAS edge and EXAFS data. *AIP Conference Proceedings* **882**, 105 (2007).

44. M. J. Frisch *et al*., *Gaussian 09, Revision A.02* (Gaussian, 2009).

45. C. B. Harris, R. M. Shelby, P. A. Cornelius, Effects of energy exchange on vibrational dephasing times in raman scattering. *Phys. Rev. Lett.* **38**, 1415–1419 (1977). doi:10.1103/PhysRevLett.38.1415

46. J. W. Petrich, J. L. Martin, D. Houde, C. Poyart, A. Orszag, Time-resolved Raman spectroscopy with subpicosecond resolution: Vibrational cooling and delocalization of strain energy in photodissociated (carbonmonoxy)hemoglobin. *Biochemistry* **26**, 7914–7923 (1987). doi:10.1021/bi00398a056 Medline